

Near-perfect infrared absorption in atomic monolayers: Approaching the fundamental optical limit

Jun-Yu Chu(楚俊宇), Cheng-Long Zhou(周承隆), Yan Wang(王妍), Yong Zhang(张勇), and Hong-Liang Yi(易红亮)
Citation: Chin. Phys. B, 2026, 35 (**8**): 084401. DOI: 10.1088/1674-1056/ae12d9
http://cpb.iphy.ac.cn; http://iopscience.iop.org/cpb

What follows is a list of articles you may be interested in

Finite element analysis of copper nanoparticles in Boger fluid: Effects of dynamic inter-particle spacing, nanolayer thermal conductivity, nanoparticles diameter, and thermal radiation over a stretching sheet

Qadeer Raza, Xiaodong Wang(王晓东), Tahir Mushtaq, Bagh Ali, and Nehad Ali Shah
Chin. Phys. B, 2025, 34 (**11**): 114402. DOI: 10.1088/1674-1056/addcbc

Cattaneo-Christov heat transfer model for tangent hyperbolic fluid with Thompson-Torian slip and melting effects

Anwar Saeed and Afrah Al-Bossly
Chin. Phys. B, 2025, 34 (**9**): 094404. DOI: 10.1088/1674-1056/add90a

Experimental study on the regulation of radiative heat flux by coating SiC film

Haifeng Xia(閤海峰) and Huihui Sun(孙慧慧)
Chin. Phys. B, 2025, 34 (**5**): 054402. DOI: 10.1088/1674-1056/adbee0

Preparation and cooling performance analysis of double-layer radiative cooling hybrid coatings with TiO_2/SiO_2/Si_3N_4 micron particles

Yang-Chun Zhao(赵洋春) and Yong-Min Zhou(周勇敏)
Chin. Phys. B, 2023, 32 (**11**): 114401. DOI: 10.1088/1674-1056/acdac0

Tuning infrared absorption in hyperbolic polaritons coated silk fibril composite

Lihong Shi(史丽弘) and Jiebin Peng(彭洁彬)
Chin. Phys. B, 2022, 31 (**11**): 114401. DOI: 10.1088/1674-1056/ac8cdc

---

Near-perfect infrared absorption in atomic monolayers: Approaching the fundamental optical limit

Jun-Yu Chu(楚俊宇)[1,2], Cheng-Long Zhou(周承隆)[1,2,†], Yan Wang(王妍)[1,2], Yong Zhang(张勇)[1,2], and Hong-Liang Yi(易红亮)[1,2]

[1] *School of Energy Science and Engineering, Harbin Institute of Technology, Harbin* 150001, *China*
[2] *Key Laboratory of Aerospace Thermophysics, Ministry of Industry and Information Technology, Harbin* 150001, *China*

(Received 21 August 2025; revised manuscript received 13 October 2025; accepted manuscript online 14 October 2025)

High absorption in the mid-infrared band is essential for applications ranging from information processing to energy harvesting. Conventionally, achieving broadband absorption approaching the optical limit has required absorber thicknesses comparable to or exceeding the characteristic wavelength. By contrast, realizing such broadband infrared absorption at the atomic scale has remained exceedingly difficult. In this work, we demonstrate that a one-dimensional MXene grating system provides a platform for achieving strong infrared absorption at atomic thicknesses. The results show that an 8-nm MXene film ($\sim \lambda/1000$) patterned with a simple stripe grating is found to approach the theoretical absorption limit of 0.5 for two-dimensional films. The absorption peak wavelength is readily tuned by varying the MXene strip width, while the positions of the optical resonances are accurately captured by a Fabry–Pérot model. Power dissipation analysis further reveals that the absorption arises from resonance-driven field enhancement and establishes a direct correlation between absorption and grating periodicity. These findings demonstrate a viable strategy for atomic-scale control of thermal radiation through rationally designed nanostructures.

Keywords: thermal radiation, theoretical absorption limit, MXene, atomic thickness

PACS: 44.40.+a, 61.80.Ba, 81.05.Xj, 42.68.Ay

DOI: 10.1088/1674-1056/ae12d9 **CSTR:** 32038.14.CPB.ae12d9

1. Introduction

With the continued miniaturization of optoelectronic components, the demand for compact, high-performance infrared radiators has increased markedly,[1–6] and research at the nanoscale has gained growing significance.[7] Among candidate platforms, two-dimensional (2D) materials, including graphene,[8–10] black phosphorus,[11,12] transition-metal dichalcogenides,[13–15] topological insulators,[16] and Dirac semimetals,[17] have drawn particular attention for their ability to confine and manipulate electromagnetic fields at the nanoscale.[18,19] Meanwhile, metasurfaces have demonstrated remarkable effectiveness as a versatile manipulation platform in areas such as thermal radiation control,[20] acoustic wave regulation,[21] and metalens engineering,[22,23] among other applications. Exploiting these properties, a variety of high-efficiency infrared absorbers and emitters have been realized,[24–28] disclosing the potential of 2D systems for energy control in ultrathin geometries. However, due to the limitations of atomic thickness, the intrinsic absorption of 2D materials is weak. For instance, graphene's intrinsic absorption is limited to 2.3% by its atomic thickness,[29] restricting its integration into truly compact devices. To further enhance absorption, diverse strategies have been explored, including localized and delocalized plasmon resonances,[30–32] guided-mode resonance,[33,34] magnetic resonance,[35,36] attenuated total reflection,[37] coherent illumination with counter-propagating beams,[38] Fano resonance,[39,40] and symmetry-protected bound states in the continuum.[20,41,42] For example, Zhao *et al.*[43,44] studied the combination of graphene with metallic gratings and found that the localized resonances (*i.e.*, magnetic polaritons) in the metal gratings could couple with plasmon resonances in graphene ribbons, significantly enhancing absorption in graphene. Lin *et al.*[45] achieved approximately 85% absorption across the solar spectrum (300 nm–2500 nm) using 90-nm-thick graphene metamaterials. Jin *et al.*[24] integrated a monolayer graphene on top of a composite silicon grating, utilizing a toroidal dipole bound state in the continuum (TD-BIC) to achieve absorption approaching the intrinsic limit (50%) at the desired wavelength. Further increasing the absorption required the introduction of a metallic back reflector. Elrafei *et al.*[18] artificially stacked WS2 monolayer semiconductors into superlattices using three different spacer layer schemes to surpass the optical absorption limit of a single WS2 layer (16% absorption on an ideal substrate). Imran *et al.*[25] proposed a polarization-insensitive scheme based on a graphene-hBN van der Waals heterostructure. This structure involves alternately stacking multiple layers of graphene and hBN, with the core idea being to utilize the anisotropic dielectric properties of hBN (which supports surface phonon

[†]Corresponding author. E-mail: zhouchenglong@hit.edu.cn

© 2026 Chinese Physical Society and IOP Publishing Ltd. All rights, including for text and data mining, AI training, and similar technologies, are reserved.

polaritons) and the tunable conductivity of graphene to achieve perfect absorption. Dai *et al.*[46] reported that when configured as double-sided emitters, ultrathin MXene films could achieve absorption approaching the intrinsic thin-film limit (50%) in the 5 μm–16 μm band. Integrating this double-sided emitter into a cavity to form a single-sided emitter, based on Fabry–Pérot resonance and critical coupling effects, resulted in an emissivity approaching unity at a wavelength of 10.8 μm. Collectively, these studies highlight the promising potential of 2D materials for infrared energy management in highly compact architectures.

Yet in nearly all such demonstrations, the enhanced performance has not been achieved by the 2D layer alone but through coupling with external media, which increases the effective thickness of the absorber.[1,8,18,24,25,43–48] However, this has the effect of weakening the advantages of two-dimensional systems at the atomic scale. This raises a central question: can a 2D material, by virtue of its intrinsic electromagnetic confinement, alone absorb and confine infrared radiation within only a few nanometres, thereby approaching the intrinsic limit?

Recent advances in synthesis have brought 2D transition-metal carbonitrides (MXenes) to the fore as promising candidates.[26,49–51] MXenes exhibit extremely high carrier densities ($\sim 10^{21}$ cm^{-3}), ultrashort relaxation times (~ 10 fs), and distinctive in-plane and interlayer transport, which together yield exceptional optical responses.[49] Indeed, Zhao *et al.*[49] have demonstrated absorption at the intrinsic thin-film limit across 0.5 THz–10 THz using MXene layers only 10-nm thick. Building on these properties, we investigate an ultrathin MXene-grating absorber capable of reaching the absorption limit of 2D systems in the mid-infrared. The device, consisting of periodically arranged MXene strips with 8-nm-thick, achieves enhanced absorption through interference of surface plasmon polaritons confined within the strips. We show that the absorber sustains peak absorption approaching the intrinsic thin-film limit across a range of 3 μm–20 μm. Its spectrum is tunable via strip width and grating geometry, and the two principal resonances can be quantitatively described by a Fabry–Pérot model. Notably, the design retains absorption above 40% even at incident angles up to 60° and is largely insensitive to the substrate, underscoring its robustness for practical implementation.

2. Method

We consider the ultrathin absorber illustrated in Fig. 1(a), in which the active layer is an atomically thin $Ti_3C_2T_x$ MXene strip array. The structure is periodic along the x-direction with period Λ, extends infinitely along y, and has a thickness h along z. All electromagnetic simulations were performed using Lumerical FDTD Solutions software. For the MXene strip array studied in this paper, due to the continuous translational symmetry along the y-axis, a 2D model in the xz-plane was used for simulations. Periodic boundary conditions were applied in the x-direction, a Perfectly Matched Layer (PML) was used in the z-direction, and the light source was set as a plane wave. The directions of the x, y, and z axes mentioned here correspond to those indicated in Fig. 1(a). The structure of the array cell under consideration consists of an MXene strip, the width of which is designated by w, and a vacuum groove, the width of which is designated by g, such that the period Λ is given by the expression $(w+g)$. Here, the substrate of the MXene array is first set to resin with a 10-nm thickness to demonstrate the exceptional absorption characteristics of this 2D system. In the following sections, we will also show its spectral characteristics under different substrate conditions. As shown later, the absorber's response is largely insensitive to the substrate, underscoring the robustness of the design.

For MXene assemblies in nanometer-sized flakes, free carriers within the flakes can scatter at flake edges and grain boundaries. The dielectric constant of MXene films can be fitted using the Drude–Smith model[49]

$$\varepsilon(\omega) = 1 + \frac{\mathrm{i}\sigma(\omega)}{\omega\varepsilon_0 h}, \tag{1}$$

$$\sigma(\omega) = \frac{\sigma_0}{1-\mathrm{i}\omega\tau}\left(1+\frac{c}{1-\mathrm{i}\omega\tau}\right). \tag{2}$$

In the formula, ω denotes the angular frequency, ε_0 represents the vacuum permittivity, σ is the conductivity of MXene, σ_0 and τ are the direct current (DC) conductivity and carrier scattering time, respectively, and the parameter c characterizes the probability of electron backscattering. The fitting parameters for MXene films of different thicknesses are presented in Table 1.[49] For instance, the fitting parameters for an 8-nm-thick MXene film are $\tau = 10.73$ fs, $c = -0.76$, $\sigma_0 = 15.06$ mS. In the mid-infrared band considered in this paper, the permittivity of the resin can be expressed as $\varepsilon_r = 2.45$.[52] The absorption $A(\lambda)$ of the absorber is calculated by $A(\lambda) = 1R(\lambda)$–$T(\lambda)$, where $R(\lambda)$ denotes the reflectance, $T(\lambda)$ represents the transmittance, and λ is the wavelength.

Table 1. MXene physical property fitting parameters.

Thickenss (nm)	τ (fs)	c	σ_0 (mS)
3.0	9.62	–0.82	6.16
6.4	10.61	–0.79	12.26
8.0	10.73	–0.76	15.06
10.0	10.98	–0.72	16.14

3. Results and discussion

The absorption spectra of MXene absorbers with varying thicknesses are shown in Fig. 1(b) for structural param-

eters $w = g = 2$ μm. Distinct resonant absorption is observed across all thicknesses, with absorption increasing as the MXene becomes thicker, accompanied by a systematic blue shift of the resonance peak. As indicated in Fig. 1(b), an 8-nm-thick MXene film suffices to reach the theoretical absorption limit of 2D materials; accordingly, this thickness has been adopted for the grating layer in the present study. For context, Table 2 summarizes recent progress in ultrathin absorbers;[1,18,25,26,45,48,49,53–55] for data where the original reports did not specify the thickness of the highly reflective substrate, the symbol '>' is used in the table. The proposed MXene grating demonstrates performance at the optical limit, enabled primarily by the exceptionally high electron density of MXene, which sustains robust surface plasmon resonances. By contrast, a 3-nm-thick MXene film remains well below the absorption limit, reflecting the diminished electron surface density at such small thickness (The electron surface densities for 8-nm and 3-nm thicknesses are $N_{8\ \mathrm{nm}} = 1.18 \times 10^{15}$ cm^{-2} and $N_{3\ \mathrm{nm}} = 0.69 \times 10^{15}$ cm^{-2},[49] respectively).

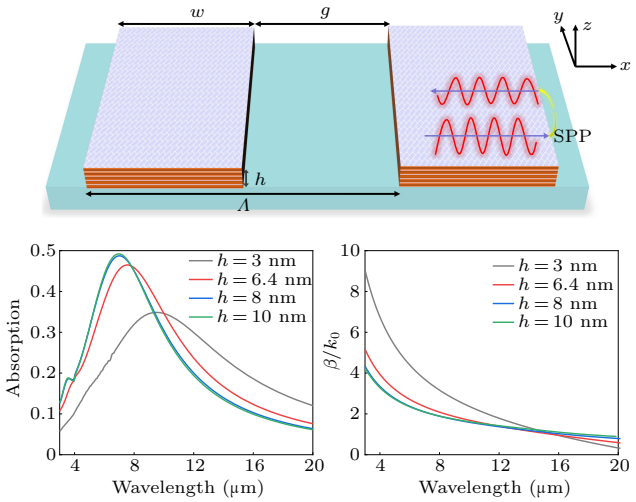


Fig. 1. (a) Schematic diagram of the considered MXene absorber, where the top layer is an atomic-thin MXene strip array periodic in the x-direction with a period of Λ and thickness h ($h = 8$ nm unless otherwise specified). The MXene strip width is w, and the vacuum groove width is g. The lower layer (light green) is composed of resin, silicon, or air. (b) Absorption spectra of MXene absorbers with different thicknesses. For all cases, $w = g = 2$ μm and $\Lambda = 4$ μm were adopted. (c) Mode indices of surface plasmons in MXene films with different thicknesses, derived from Eq. (3).

Using the dielectric function of MXene, one can describe the dispersion of the surface plasmon polariton in the atomically thin MXene[43,56]

$$\frac{\varepsilon_1}{\sqrt{\beta^2 - \varepsilon_1 k_0^2}} + \frac{\varepsilon_2}{\sqrt{\beta^2 - \varepsilon_2 k_0^2}} = -\frac{\mathrm{i}\sigma}{\omega \varepsilon_0}, \tag{3}$$

where $k_0 = \omega/c_0$ is the vacuum wavevector, with c_0 being the light speed in vacuum, β is the wavevector for the plasmon, ε_0 is the permittivity of vacuum, and ε_1 and ε_2 are the dielectric functions of the media that are on each side of MXene. The mode index is defined as $\mathrm{Re}(\beta)/k_0$.[56] As shown in Fig. 1(c), MXene films with a thickness of 3 nm have higher plasma wavevectors within a wavelength of 16 μm.

The absorption spectrum of the ultrathin MXene absorber can be tuned by engineering the strip geometry. We considered two scenarios: (i) fixing the period at $\Lambda = 4$ μm while varying the groove dimensions, and (ii) fixing the groove width at $g = 2$ μm while increasing the period to adjust the MXene strip width. As shown in Fig. 2(a), for a fixed period of 4 μm, the peak absorption wavelength undergoes a progressive blue shift with increasing groove width. Conversely, Fig. 2(d) shows that for $g = 2$ μm, the peak absorption wavelength red shifts as the period increases. In both cases, two distinct resonant absorption peaks emerge, as further illustrated in Figs. 2(b) and 2(e). These resonance characteristics are well described by a Fabry–Pérot model: surface plasmon polaritons excited within the MXene strips partially reflect at the strip edges and scatter into free-space modes. Multiple reflections of these surface plasmon polaritons (SPPs) lead to an interference effect, generating resonance-enhanced near fields. Consequently, the MXene strips function as Fabry–Pérot resonators.[57,58] The resonance condition can be expressed as[56,58–60]

$$\Delta\varphi + Re(\beta)\, w = m\pi, \tag{4}$$

here, m denotes the resonance order, $\Delta\varphi$ is the reflection phase at the strip edges, and w is the width of the MXene strip. Under normal incidence, only odd values of m give rise to resonance, since plasmons launched from the two edges are out of phase; for even m, their interference is strictly destructive, hindering resonance.[43,60] Figure 2(b) illustrates the strip-resonance phenomenon as the groove width approaches the array period, with the Fabry–Pérot predictions shown as dashed lines. For the fundamental resonance ($m = 1$), a phase shift of $\Delta\varphi = -0.2\pi$ is adopted, while for the third-order resonance ($m = 3$), $\Delta\varphi$ is $-\pi$. Similarly, Fig. 2(d) depicts the resonance evolution with increasing period, and the corresponding Fabry–Pérot predictions show excellent agreement with numerical simulations. As can be seen from the above results and analysis, treating MXene strips as Fabry–Pérot resonators and using Eq. (4) can well describe the resonant wavelengths of the absorber and the shift behavior of the resonant wavelengths with absorber parameters. The results in Fig. 2 show that the absorption spectrum is highly dependent on the geometric parameters. To quantitatively elucidate this tunability and the physical mechanism behind achieving near-perfect absorption, we employed Temporal Coupled–Mode Theory (TCMT). TCMT is widely used in the analysis and design of various absorbers,[20,24,56,61,62] providing a universal and rigorous theoretical framework for predicting the spectral absorption near strip resonances. Within TCMT, the absorption of a leaky mode in a two-port system is expressed as[24]

$$A = \frac{2\gamma_0\gamma}{(\omega - \omega_0)^2 + (\gamma_0 + \gamma)^2}, \tag{5}$$

where ω_0 denotes the resonance frequency of the structure, γ_0 is the dissipative loss rate, and γ is the radiative decay rate. From Eq. (5), we observe that when the system is driven at resonance $\omega = \omega_0$ and $\gamma = \gamma_0$, the absorption is enhanced to 50%, which is known as the critical coupling condition.[24,56,63] The influences of the background permittivity, material properties, and structural parameters are all reflected in these coupled-mode parameters.[56,63]

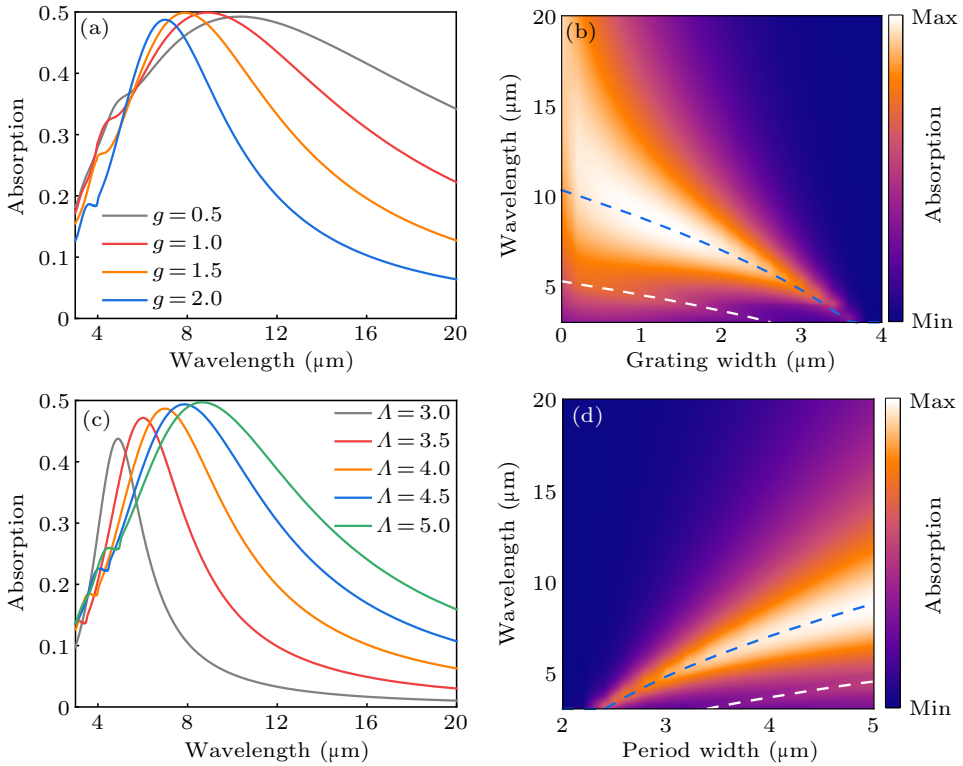


Fig. 2. (a) Absorption spectra of MXene absorbers with different groove widths at $\Lambda = 4$ μm. (b) Absorption contour plots of MXene absorbers with different groove widths at $\Lambda = 4$ μm fixed. (c) Absorption spectra of MXene absorbers with different periods at $g = 2$ μm. (d) Absorption contour plots of MXene absorbers with different periods at $g = 2$ μm. The dashed lines in panels (c) and (d) represent fitting results of the Fabry–Pérot model given by Eq. (4), in which the blue and white dashed lines correspond to the $m = 1$ and $m = 3$ resonance fittings, respectively.

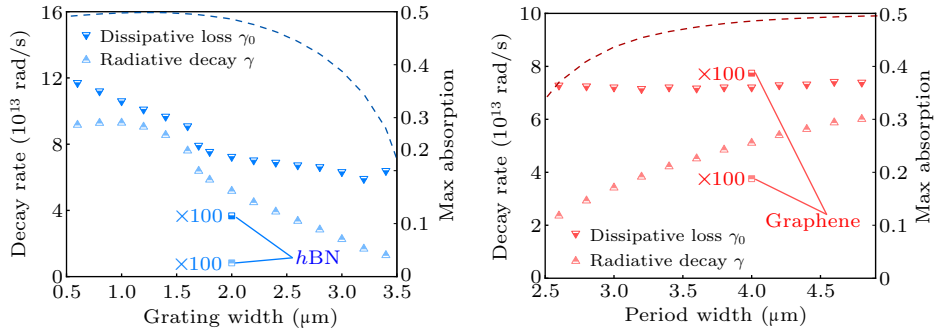


Fig. 3. (a) Coupling parameters of TCMT in Fig. 2(a) ($\Lambda = 4$ μm). (b) Coupling parameters of TCMT in Fig. 2(c) ($g = 2$ μm). The blue and red boxes denote the coupling parameters of hBN and graphene absorbers, respectively, which adopt the same structure as MXene with $w = g = 2$ μm, $\Lambda = 4$ μm, and $h = 8$ nm. Here, parameter regions are excluded where the absorption is extremely low and resonant interference is severely compromised due to excessively large or small proportions of the air groove or MXene strip.

Figure 3 illustrates how the structural parameters of the absorber influence the loss rates. By varying the widths of strip and groove, the coupling regime can be tuned from undercoupling to near-critical coupling. As shown in Fig. 3(b), the dissipative loss rate γ_0 remains essentially independent of the period and can be regarded as constant when the vacuum groove width is fixed, thereby simplifying the optimization of absorber performance. Compared with MXene, the relatively lower carrier densities of other 2D materials suppress the strength of mid-infrared plasmons. They may require more delicate structural designs to approach the absorption limit. For instance, graphene and hBN strip absorbers with the same structural dimensions and thickness as the MXene absorber (as listed in Table 2) failed to approach the absorption limit. Specifically, the loss rates are $\gamma_{\text{graphene}-0} = 7.74 \times 10^{11}$ rad/s and $\gamma_{\text{graphene}} = 3.76 \times 10^{11}$ rad/s for graphene, and $\gamma_{\text{hBN}-0} = 3.67 \times 10^{11}$ rad/s and $\gamma_{\text{hBN}} = 8.27 \times 10^{10}$ rad/s for hBN, confirming that both systems remain undercoupled under these specific conditions.

Table 2. Recent progress in ultrathin absorbers; the symbol ">" indicates data for which the thickness of the reflective substrate was not explicitly specified in the original literature. The last row shows the results of graphene or hBN absorbers, which have the same structural parameters as the MXene absorber adopted in this study.

Material	Thickness	IR band	Absorption	Ref.
Graphene	330 nm	VIS	0.28	[1]
WS2	> 58.5 nm	VIS	0.31	[18]
Graphene, hBN	200 μm	MIR	0.99	[25]
MXene	20 nm	FIR	0.5	[26]
Graphene	270 nm	NIR	0.85	[45]
TIN	> 120 nm	MIR	0.48	[48]
MXnen	10 nm	FIR	0.5	[49]
Graphene	280 nm	NIR	0.42	[53]
Graphene	1400 nm	MIR	0.99	[54]
Graphene, hBN	10 nm (applied magnetic)	MIR	0.36	[55]
MXnen	8 nm	MIR	0.5	**this work**
Graphene/hBN	8 nm	MIR	0.44/0.36	

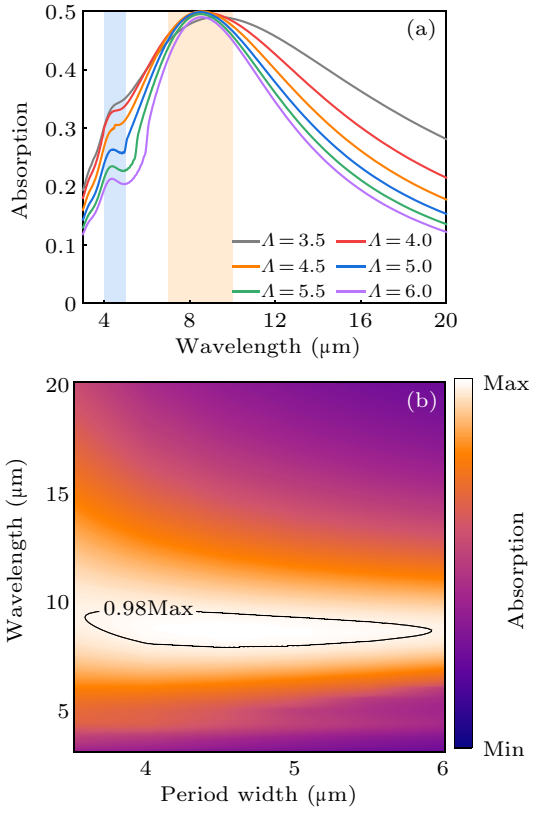


Fig. 4. (a) Absorption spectra at different periods for MXene grating at $w = 3$ μm. (b) Absorption contour map of MXene grating as a function of wavelength and period while fixing MXene strip width at 3 μm.

In Fig. 4(a), we present the evolution of the absorption spectrum as a function of wavelength and period while fixing MXene strip width at 3 μm. Two resonant absorption peaks emerge at $\lambda_1 = 8.66$ μm and $\lambda_2 = 4.45$ μm, located within the atmospheric transparency windows of 8 μm–13 μm and 3 μm–5 μm, respectively. These spectral features provide valuable design principles for applications in radiative cooling and thermal camouflage. Figure 4(b) further reveals a broadband high-absorption plateau (absorption > 0.49) across the mid-infrared, where the absorption shows weak dependence on the unit period size. This behavior accords well with Fabry–Pérot predictions: both the fundamental and third-order resonance peaks remain robust to variations in period. Moreover, reducing the period substantially enhances mid-infrared absorption. Using 40% absorption as a benchmark, the high-absorption bandwidth is 4.2 μm at $\Lambda = 6$ μm, but broadens to 8.6 μm when $\Lambda = 3.5$ μm, nearly doubling the bandwidth. This pronounced increase demonstrates that smaller periods enable stronger plasmon-enhanced electromagnetic absorption.

To gain deeper insight into the plasmonic resonance–enhanced absorption in the MXene grating array, we have calculated the electric field intensity E at the first- and third-order resonance wavelengths, as shown in Figs. 5(a) and 5(b). The structural parameters are fixed as $w = 3$ μm, $g = 2$ μm, and $\Lambda = 5$ μm. Figure 5(a) shows the field distribution at the first-order resonance ($\lambda = 8.66$ μm), where strong field enhancement at the strip edges confirms that the MXene strips function as Fabry–Pérot resonators. This behavior arises from the constructive interference of surface plasmon polaritons reflected at the strip boundaries, giving rise to resonance-enhanced fields localized near the edges. Figure 5(c) presents the electric field distribution along the surface-normal direction, clearly demonstrating that the field is tightly confined to the MXene interface. The decay length is approximately 200 nm, a typical feature of the evanescent field of surface plasmons.[64] At the third-order resonance ($\lambda = 4.45$ μm), shown in Fig. 5(b), the field profile exhibits similar edge-localized enhancement, though the peak field intensity is weaker than at $\lambda = 8.66$ μm. Notably, the field distribution within the strip displays two distinct maxima, reflecting the constructive superposition of higher-order plasmon modes, a feature absent in the fundamental resonance. This difference originates from the phase shifts experienced by surface polaritons upon reflection at the strip edges, which determine the modal structure of Fabry–Pérot resonances in the MXene array.

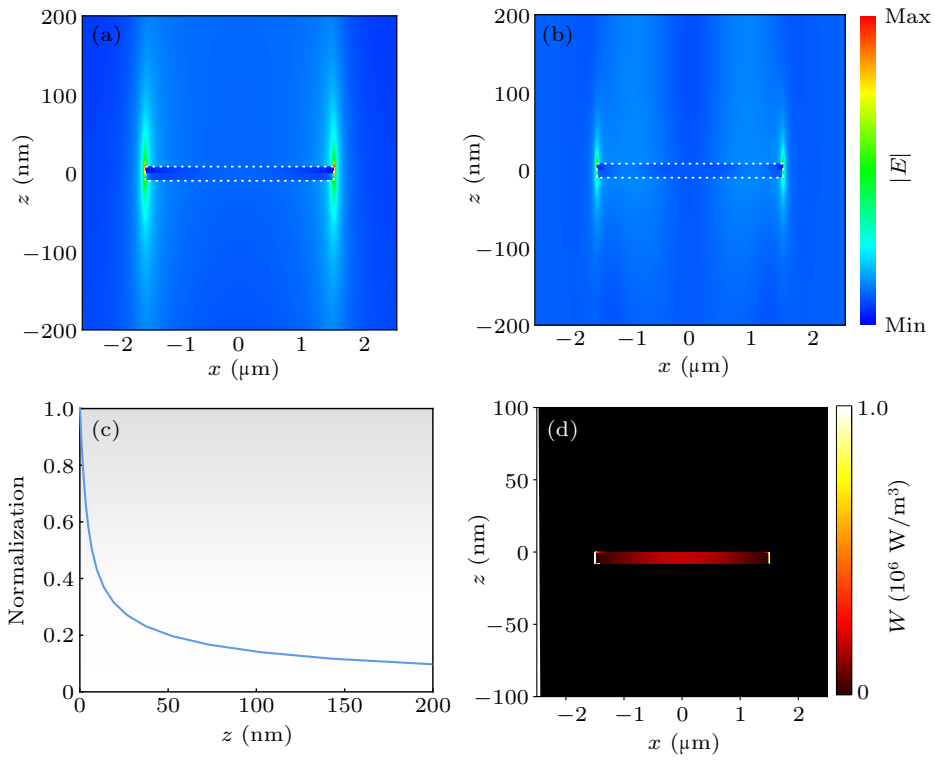


Fig. 5. (a) Electric field distribution at the first-order resonance peak. (b) Electric field distribution at the third-order resonance peak. (c) Normalized electric field intensity decay along the interface normal direction at the MXene edge. (d) Power dissipation distribution at the first-order resonance peak calculated using Eq. (6). The structural parameters of the MXene absorber are $w = 3$ μm, $\Lambda = 5$ μm.

To further quantify the local absorption within the MXene strips, the power dissipation profile was calculated, which is defined as follows:[43,44]

$$W(x,z) = \frac{1}{2}\varepsilon_0 \omega \varepsilon''(x,z)\,|E(x,z)|^2, \tag{6}$$

where E is the complex electric field and ε'' is the imaginary part of the material dielectric function. It is noted that since all materials considered are non-magnetic, no magnetic losses are involved. Figure 5(d) shows the overall power dissipation profile at $\lambda = 8.66$ μm, with the detailed distribution in MXene presented in Fig. 6(a). The power dissipation profile is symmetric about the $x = 0$ plane. Directly correlated with the square of the electric field intensity, the power dissipation density at the edges of MXene strips significantly exceeds that in the central region, attributed to the localized field enhancement from surface plasmon resonance within the Fabry–Pérot resonator formed by MXene strips. The order-of-magnitude difference between edge and central regions exceeds two orders, highlighting the spatial inhomogeneity of strong field localization driven by surface plasmon resonance. The strongest surface plasmons excited at the MXene surface also lead to higher power dissipation density there compared to other regions. Similarly, the detailed power dissipation density distribution in MXene at the resonant wavelength of $\lambda = 4.45$ μm is shown in Fig. 6(b), exhibiting similar characteristics to the above case. However, due to the weakened resonance, the difference in orders of magnitude of power dissipation density between the edge and central regions contracts from over two orders of magnitude ($> 100\times$) to exceeding one but less than two orders of magnitude ($> 10\times$). Additionally, although the power dissipation density at the edges decays rapidly, reducing to near the central region's level within ~ 20 nm, the high magnitude at the edges enables a 10% absorption contribution from the edge microregion, which accounts for only 1% of the strip's cross-sectional area.

Based on the above power dissipation profile, the absorption for a given volume can be calculated by the ratio of the dissipated power within the volume to the incident power through the exposed surface area A_{sur}, as expressed by the following equation[43,44]

$$A = \frac{\iiint W(x,z)\,\mathrm{d}V}{\frac{1}{2}c_0\varepsilon_0\,|E_{\mathrm{inc}}|^2 A_{\mathrm{sur}}\cos\theta}, \tag{7}$$

where the denominator represents the product of the Poynting vector and the projected surface area at an incident angle of θ. For the 1D structure discussed in this paper, the dimension along the y-axis is neglected, and the volume integral is performed solely over the x–z plane. Considering the periodic boundary conditions of the structure, when the cross-sectional area A_{sur} of the integration region is taken as the period Λ, the integration range in the x-direction can be confined to a single period length. Based on Eq. (7), the significant negative size-dependence of the spectral absorption observed in Fig. 4(a) can be understood. Figures 6(d) and 6(c) show the power dissipation distribution at the third-order resonance peak, $z = 0$ nm

(strip surface) and $z = -4$ nm (strip center), respectively. The results reveal that the dissipation within the MXene itself is essentially identical for both structures, indicating that the difference in absorption originates from the distinct effective interaction areas determined by the periodicity ($\Lambda = 4$ μm versus $\Lambda = 5$ μm).

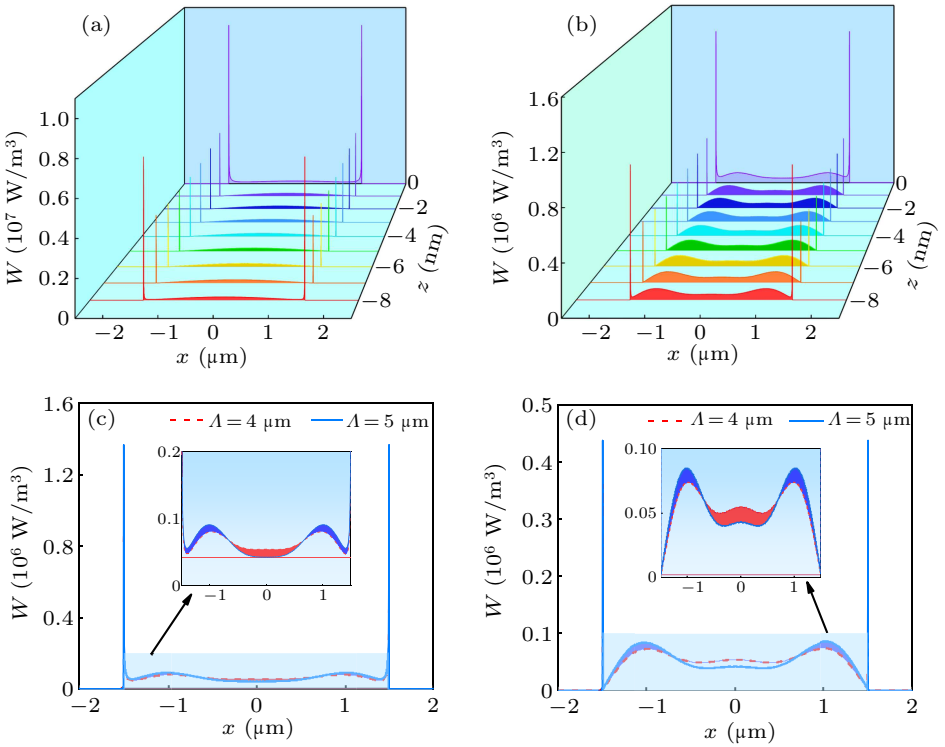


Fig. 6. Power dissipation distribution within the MXene strip at (a) the first-order resonance peak and (b) the third-order resonance peak. The structural parameters of the MXene absorber are $w = 3$ μm and $\Lambda = 5$ μm. Comparison of power dissipation distributions at the third-order resonance peak for (c) $z = 0$ nm (strip surface) and (d) $z = -4$ nm (strip center), with different periods ($\Lambda = 4$ μm versus $\Lambda = 5$ μm).

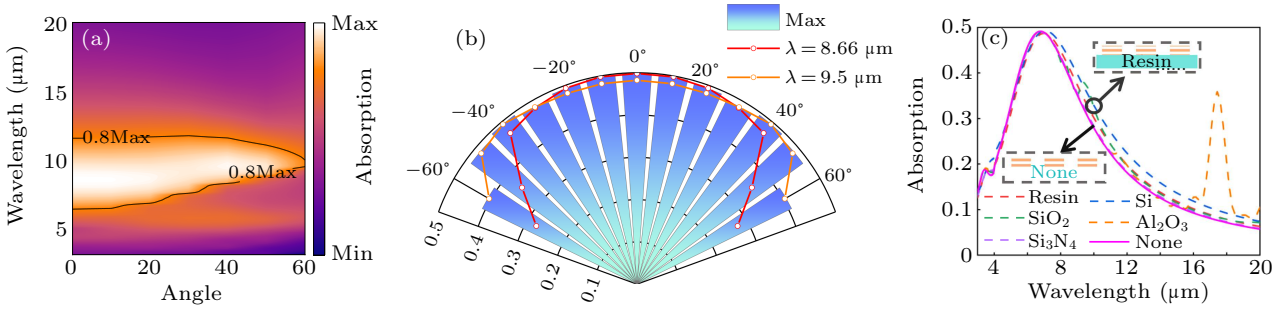


Fig. 7. (a) Absorption spectra under different incident angles. (b) Redshift of the peak absorption wavelength. The structural parameters of the MXene absorber are $w = 3$ μm and $\Lambda = 5$ μm. (c) Influence of substrates on the absorber, with the same structure as in Fig. 1(b).

Figure 7(a) shows the absorption spectra under oblique incidence, revealing that such an absorber sustains strong infrared absorption across a broad angular range. Even at $\theta = 50°$, the maximum absorption remains near the theoretical limit, exceeding 48%. For larger angles ($\theta = 60°$), a notable reduction is observed, yet the absorption still surpasses 40% [see Fig. 7(b)]. With increasing incident angle, the high-absorption bandwidth narrows, accompanied by a systematic red shift of the resonance peak from 8.66 μm at normal incidence to 9.5 μm. A pronounced angular dependence emerges when θ exceeds 30°, as shown in Fig. 7(b). When the illumination is oblique, the symmetry of the system is broken, introducing an additional phase difference between the SPPs excited at the two edges. Analysis based on Eq. (4) indicates that this leads to a redshift of the resonance wavelength. Furthermore, the excitation efficiency for the fundamental resonance decreases under oblique incidence, resulting in a reduction of the high-absorption bandwidth. Additionally, factors such as the excitation of SPPs, the reflection phase, and higher-order diffraction under oblique incidence also influence the absorption performance. We further examined the role of substrate materials [see Fig. 7(c)], finding only negligible influence: The absorption peak and resonance wavelength remain almost unaffected when different materials are used as the substrate, with fluctuations in the absorption peak not exceeding 0.003 and shifts in the resonance wavelength being

less than 0.2 μm. Although an additional absorption peak appears due to the high loss of Al_2O_3 in the 16 μm–18 μm band, it has no impact on the resonance absorption dominated by the MXene strips. This confirms the robustness of the design strategy across diverse non-metallic substrates. Remarkably, even in the absence of a substrate, the 8-nm-thick MXene-grating array achieves the theoretical absorption limit, thereby overcoming the thickness constraints inherent to conventional absorbers.

4. Conclusions

In this work, we demonstrate that a 1D MXene-grating array can realize strong infrared absorption within only a few nanometers of thickness, relying solely on its intrinsic surface electromagnetic modes and without recourse to additional thick materials. Remarkably, at a thickness of merely 8 nm, such MXene-grating array can approach the fundamental absorption limit of two-dimensional systems (50%), outperforming conventional platforms such as graphene and hBN. Beyond high absorption, the MXene-grating array exhibits exceptional spectral tunability: by precisely engineering the strip width and grating period to tailor Fabry–Pérot resonances, absorption peaks can be tuned over a spectral span approaching 10 μm. To elucidate the physical origin of these properties, we employed temporal coupled-mode theory, which reveals exceptionally high dissipation and radiation loss rates, and power dissipation analysis, which uncovers striking spatial inhomogeneity, edge regions constituting only $\sim 1\%$ of the strip cross-section contribute up to 10% of total absorption through localized field enhancement. The absorber further displays robust angular tolerance, sustaining $> 48\%$ absorption at 50° incidence and $> 40\%$ at 60°, with negligible dependence on substrate choice. Collectively, these attributes overcome long-standing limitations of conventional 2D absorbers by eliminating the need for thick dielectric spacers or reflective substrates while preserving atomic-scale thinness, thereby unlocking new possibilities for radiative cooling, thermal camouflage, and tunable thermal emission technologies based on ultra-thin materials.

It should be noted that while this work demonstrates the exceptional infrared absorption capability of MXene gratings at the atomic scale, their absorption bandwidth is limited, and they face challenges in environmental stability for practical applications. Future research directions could include optimizing MXene material synthesis processes, designing multilayer MXene structures, and creating composites of MXene with other 2D materials to further address existing absorption performance bottlenecks. Furthermore, unprotected MXene films may undergo oxidation in air, leading to performance degradation. Future studies should explore effective stabilization strategies, such as surface passivation[65] and functional group engineering[66] for oxidation resistance, to simultaneously maintain their excellent absorption performance and long-term stability.

Acknowledgements

Project supported by the National Natural Science Foundation of China (Grant Nos. U22A20210, 52522604, and 523B2060), the Postdoctoral Fellowship Program of CPSF (Grant No. GZB20240951), the China Postdoctoral Science Foundation (Grant No. 2025M774311), and the Funding for Postdoctoral Candidates in Heilongjiang Province, China (Grant No. AUGA41100088248).

References

[1] Fan Y S, Zhu Z H, Zhang J F, Xu W, Wu F, Yuan X D, Guo C C and Qin S Q 2022 *Opt. Express* **30** 41110
[2] Novoselov K S, Geim A K, Morozov S V, Jiang D, Zhang Y, Dubonos S V, Grigorieva I V and Firsov A A 2004 *Science* **36** 666
[3] Bonaccorso F, Sun Z, Hasan T and Ferrari A C 2010 *Nat. Photon.* **4** 611
[4] Dorgan V E, Behnam A, Conley H J, Bolotin K I and Pop E 2013 *Nano Lett* **13** 4581
[5] Lee H G, Wei X D, Kysar J W, Hone J, Wei X D, Kysar J W and Hone J 2008 *Science* **321** 385
[6] Zhang C X, Li T J, Xu L J and Huang J P 2023 *Chin. Phys. Lett.* **40** 054401
[7] Zhang J, Zhang H C and Zhang G 2024 *Front. Phys.* **19** 23204
[8] Luo W, Abbasi S A, Li X J, Ho H P and Yuan W 2025 *Opt. Laser Technol.* **180** 111460
[9] Zhao Y J, Dong C Y, Sang S X, Dong J Y, Xu X L and Wang Y X 2022 *Optoelectron. Lett.* **18** 360
[10] Liu C, Lin J P, Wu N, Weng C X, Han M R, Liu W, Liu J R and Zeng Z H 2024 *Carbon* **223** 119017
[11] Wang B S, Wang T Y, Liu Y F and Yu K 2024 *Curr. Appl. Phys.* **57** 26
[12] Hajian H, Rukhlenko I D, Hanson G W and Ozbay E 2022 *Photon. Nanostruct.* **50** 101020
[13] Li D, Zhang W J, Suo P, Chen J M, Sun K W, Zou Y Q, Ma H, Lin X, Yan X N, Zhang S F, Li B and Ma G H 2022 *J. Phys. Chem. Lett.* **13** 2757
[14] You S W, Shao Z Y, Guo X, Jiang J J, Liu J X, Wang K, Li M J, Ouyang F P, Deng C Y, Song F, Sun J T and Huang H 2023 *Chin. Phys. B* **32** 017901
[15] Zhang W J, Liu Q S, Cheng B, Chao M H, Xu Y and Song G F 2023 *Chin. Phys. B* **32** 034211
[16] Nivedan A and Kumar S 2023 *J. Phys. D: Appl. Phys.* **56** 10956
[17] Dai Z J, Manjappa M, Yang Y K, Tan T C W, Qiang B, Han S, Wong L J, Xiu F C, Liu W W and Singh R 2021 *Adv. Funct. Mater.* **31** 2011011
[18] Elrafei S A, Heijnen L M, Godiksen R H and Curto A G 2024 *ACS Photon.* **11** 2587
[19] Meng X Q, Qin C B, Liang X L, Zhang G F, Chen R Y, Hu J Y, Yang Z C, Huo J Z, Xiao L T and Jia S T 2024 *Front. Phys.* **19** 53601
[20] Xu G Z, Xue Z Q, Fan J X, Lu D, Xing H Y, Shum P P, Zhou Y and Cong L Q 2024 *Adv. Mater.* **36** 2406526
[21] Hao Z L, Chen H J, Yin Y H, Qiu C W, Zhu S and Chen H Y 2024 *Front. Phys.* **19** 42202
[22] Chen Y, Zhang S M, Tian Y, Li C X, Huang W L, Liu Y X, Jin Y X, Fang B, Hong Z and Jing X F 2024 *Opto-Electronic Advances* **7** 240095
[23] Chen P, Fang B, Li J, Wang Z, Li C and Jing X 2023 *J. Lightwave Technol.* **41** 7121
[24] Jin R, Huang L J, Zhou C B, Guo J Y, Fu Z C, Chen J, Wang J, Li X, Yu F L, Chen J, Zhao Z Y, Chen X S, Lu W and Li G H 2023 *Nano Lett.* **23** 9105
[25] Imran M, Musa M Y, Rauf S, Lu D J, Li R J and Tian Y B 2024 *Sci. Rep.* **14** 10068
[26] Fei Y, Wang Q X, Wang F, Zhang G Z, Hu M, Ding T P, Zhao T and Xiao X 2025 *Infomat* **7** 12654

[27] Huang L J, Li G Q, Gurarslan A, Yu Y L, Kirste R, Guo W, Zhao J J, Collazo R, Sitar Z, Parsons G N, Kudenov M and Cao L Y 2016 *ACS Nano* **10** 7493

[28] Yao Y, Shankar R, Kats M A, Song Y, Kong J, Loncar M and Capasso F 2014 *Nano Lett.* **14** 6526

[29] Nair R R, Blake P, Grigorenko A N, Novoselov K S, Booth T J, Stauber T, Peres N M R and Geim A K 2008 *Science* **320** 1308

[30] Li H J, Ji C S, Ren Y Z, Hu J G, Qin M and Wang L L 2019 *Carbon* **141** 481

[31] Deng G S, Song X L, Dereshgi S A, Xu H Q and Aydin K 2019 *Opt. Express* **27** 23576

[32] Hou T, Ge Y X, Xue S W and Chen H Y 2024 *Front. Phys.* **19** 32201

[33] Qing Y M, Ma H F, Ren Y Z, Yu S and Cui T J 2019 *Opt. Express* **27** 5253

[34] Park G C and Park K 2021 *Opt. Express* **29** 7307

[35] Zhang Y, Meng D J, Li X, Yu H H, Lai J J, Fan Z Y and Chen C H 2018 *Opt. Express* **26** 30862

[36] Fan Y S, Guo C C, Zhu Z H, Xu W, Wu F, Yuan X D and Qin S Q 2018 *Sci. Rep.* **8** 13709

[37] Zhu J F, Li C W, Ou J Y and Liu Q H 2019 *Carbon* **142** 430

[38] Feng X, Zou J L, Xu W, Zhu Z H, Yuan X D, Zhang J F and Qin S Q 2018 *Opt. Express* **26** 29183

[39] Ferreira A, Peres N M R, Ribeiro R M and Stauber T 2012 *Phys. Rev. B* **85** 115438

[40] Liu F, Chen L, Guo Q, Chen J, Zhao X and Shi W 2015 *Opt. Express* **23** 21097

[41] Wang X, Duan J Y, Chen W Y, Zhou C B, Liu T T and Xiao S Y 2020 *Phys. Rev. B* **102** 155432

[42] Zhang R, Li X C and Liu Q H 2024 *Appl. Phys. Lett.* **125** 211701

[43] Zhao B and Zhang Z M 2015 *ACS Photon.* **2** 1611

[44] Zhao B, Zhao J M and Zhang Z M 2014 *Appl. Phys. Lett.* **105** 031905

[45] Lin H, Sturmberg B C P, Lin K T, Yang Y Y, Zheng X R, Chong T K, de Sterke C M and Jia B H 2019 *Nat. Photon.* **13** 270

[46] Dai C Z, Zhu H Z, Qin R, Qin B, Zhao M, Ghosh P, Qiu M and Li Q 2025 *Optica* **12** 685

[47] Jing Z, Sang T, Ouyang S Y, Lu J J and Wang Y K 2025 *Opt. Lett.* **50** 3253

[48] Luk T S, Xu G P, Ross W, Nogan J N, Scott E A, Ivanov S, Niculescu O, Mitrofanov O and Harris C T 2022 *Appl. Phys. Lett.* **121** 234101

[49] Zhao T, Xie P Y, Wan H J, Ding T P, Liu M Q, Xie J L, Li E E, Chen X Q, Wang T W, Zhang Q, Wei Y Y, Gong Y B, Wen Q Y, Hu M, Qiu C W and Xiao X 2023 *Nat. Photon.* **17** 622

[50] Han M K, Zhang D Z, Shuck C E, McBride B, Zhang T, Wang R C, Shevchuk K and Gogotsi Y 2023 *Nat. Nanotechnol.* **18** 373

[51] Han M K and Gogotsi Y 2023 *Carbon* **204** 17

[52] Shen Z L, Li S N, Xu Y F, Yin W, Zhang L Y and Chen X F 2021 *Phys. Rev. Appl.* **16** 014066

[53] Chen J, Chen S Y, Gu P, Yan Z D, Tang C J, Xu Z J, Liu B and Liu Z Q 2020 *Carbon* **162** 187

[54] Chen H, Chen Z H, Yang H, Wen L H, Yi Z, Zhou Z G, Dai B, Zhang J G, Wu X W and Wu P H 2022 *RSC Adv.* **12** 7821

[55] Nedoliuk I O, Hu S, Geim A K and Kuzmenko A B 2019 *Nat. Nanotechnol.* **14** 756

[56] Zhao B, Song J H, Brongersma M and Fan S H 2021 *ACS Photon.* **8** 872

[57] Barnard E S, White J S, Chandran A and Brongersma M L 2008 *Opt. Express* **16** 16529

[58] Nikitin A Y, Low T and Martin-Moreno L 2014 *Phys. Rev. B* **90** 041407

[59] Della Valle G, Sondergaard T and Bozhevolnyi S I 2008 *Opt. Express* **16** 6867

[60] Du L P, Tang D Y and Yuan X C 2014 *Opt. Express* **22** 22689

[61] Piper J R and Fan S H 2014 *ACS Photon.* **1** 347

[62] Sun K L, Cai Y J, Huang L J and Han Z H 2024 *Nat. Commun.* **15** 4019

[63] Zhao Z X, Guo C and Fan S H 2019 *Phys. Rev. A* **99** 033839

[64] Guo X D, Li N, Wu C C, Dai X K, Qi R S, Qiao T Y, Su T Y, Lei D D, Liu N S, Du J L, Wang E G, Yang X X, Gao P and Dai Q 2022 *Adv. Mater.* **34** 2201120

[65] Khalid Z, Hadi F, Xie J, Chandrabose V and Oh J M 2025 *Small* **21** 2407856

[66] Tian Y M, Hou P F, Zhang H W, Xie Y, Chen G, Li Q, Du F, Vojvodic A, Wu J Z and Meng X 2024 *Nat. Commun.* **15** 10099